Solvent-free and long-cycling garnet-based lithium-metal batteries

Jiameng Yu
ShanghaiTech University
Chang Zhang
ShanghaiTech University https://orcid.org/0000-0003-0404-2446
Cong Wu
ShanghaiTech University
Ran Wei
ShanghaiTech University
Shaojie Chen
ShanghaiTech University https://orcid.org/0000-0003-4611-249X
Yingjie He
ShanghaiTech University
Qilin Hu
ShanghaiTech University
Wei Liu (liuwei1@shanghaitech.edu.cn)
ShanghaiTech University https://orcid.org/0000-0002-6206-8321

Article

Keywords:

Posted Date: August 17th, 2022

DOI: https://doi.org/10.21203/rs.3.rs-1924568/v1

Abstract

Solid-state batteries using ceramic solid electrolytes promise to deliver enhanced energy density and intrinsic safety. However, the challenge of integrating solid electrolytes with electrode materials limits the electrochemical performances. Herein, we report a solvent-free ceramic-based lithium-metal battery with excellent performances at a wide temperature range of 45 to 100°C, enabled by inorganic ternary salt of extreme-low eutectic point. By using garnet electrolyte with molten salts at the electrolyte|cathode interface, the Li||$LiFePO_4$ cells perform a long cycling stably with capacity retention of 81.4% after 1000 cycles at 1 C. High-voltage $LiFe_{0.4}Mn_{0.6}PO_4$ cathodes also deliver good electrochemical performance. Specifically, commercial electrode pieces with high area capacities can be adopted directly in the quasi-solid-state lithium-metal batteries. These superior performances are ascribable to the low melting point, high ionic conductivity and good thermal/electrochemical stability of the ternary salt system. Our findings provide an effective method on fabrication of solid-state batteries towards practical applications.

Introduction

The rapid development of electric vehicles and large-scale energy storages arouses huge demand for lithium-ion batteries (LIBs) with high energy density, long cycling life and intrinsic safety[1–3]. Solid-state lithium-metal batteries (SSLMBs) have been deemed as the promising candidate for their potential improvements in safety and energy density[4–6]. However, current SSLMBs have not achieved the performance goals of energy density up to 500 Wh kg^{-1} and cycling life over 1000 cycles with the retention of 80% at the cell level[7, 8]. Extensively explored inorganic solid electrolytes (ISEs), such as oxide[9, 10], sulfide[11, 12] and halide[13, 14] have achieved great progress in ionic conductivity, flame retardancy and ionic transference number but still suffer from the unsatisfactory electrochemical performance, predominantly owing to high impedances at various solid-solid interfaces in SSLMBs related to chemical incompatibility, electrochemical instability and mechanical failure[15, 16]. For garnet-type oxide electrolytes, although thermodynamic stability at interfaces is maintained relatively, the physical contact with electrodes limits the practical application, which is much more serious in the cathode side, arising from the rigid particles of cathode composites with a variety of interfaces[17–19]. Considerable efforts have been devoted to achieve an intimate electrolyte|cathode contact, such as applying liquid electrolyte or polymer as catholyte[20, 21], co-sintering[22, 23], and maintaining high pressure during cycling[24, 25]. Throughout those approaches, adding a tiny bit of liquid electrolyte or polymer buffer layer is the most effective way to decrease the interfacial impedance and achieve long cycling batteries[26]. Nevertheless, organic compounds bring risks to the intrinsic safety of the solid-state battery[27]. High temperature co-sintering could achieve intimate contact between ceramic electrolyte and cathode particles; however, serious element diffusion at the interface is accompanied[28, 29]. Besides, adding pressure control device leads to sacrificed volumetric energy density[17]. Hence, an effective strategy is still highly required.

Molten salts, referred to the melt of inorganic salts, usually come to sight in the form of eutectic system with lower melting point and have wide applications in phase change heat storage[30, 31], material synthesis[32, 33] and electrochemical energy storage[34], etc. Molten salt electrolytes have attracted much attention owing to their nonvolatility, thermal stability over the liquid electrolyte as well as high ionic conductivity achieved since solid-liquid transition occurs. Compared with organic ionic liquid with large-size organic cations, inorganic molten salts show more accessible preparation, better thermal stability and are more cost effective. Sadoway et al. reported a Li||Sb-Pb all liquid battery with LiF-LiCl-LiI molten salt electrolyte that can operate at a current of 1000 mA cm^{-2} and 450°C[35]. Recently, an interesting strategy using low-melting antiperovskite electrolyte of Li_2OHCl[36], was demonstrated as a potential system to combine with high voltage cathode and graphite/$Li_4Ti_5O_{12}$ anode through 'melt-infiltration' process at moderate temperature (~ 300°C) achieving direct solidification of the solid electrolyte into desired shape and thickness. However, it should be noted that batteries with operating temperature close to room temperature is most likely to be available for practical application.

Herein, we develop a solvent-free and high-performance Li-metal batteries based on garnet solid electrolyte and molten salts in terms of electrolyte|cathode integration. The (Li,K,Cs)FSI ternary system of eutectic transition temperature as low as 45°C is synthesized successfully. By filling a trace amount of molten salt into the pores of the cathode, the interfacial impedances both at garnet electrolyte|cathode interface and in the composite cathode decrease significantly. As a result, the quasi-solid-state Li-metal batteries (QSSLMBs) using $LiFePO_4$ (LFP) and high voltage cathode $LiFe_{0.4}Mn_{0.6}PO_4$ (LFMP) can deliver superior electrochemical performances at a wide temperature range of 45 to 100°C. Specially and interestingly, commercial cathode with high areal capacities can be directly used.

Results And Discussion

Synthesis and characterization of molten salts and garnet electrolyte

To avoid volatile solvent and flammable organics, the inorganic (Li,K,Cs)FSI ternary system was introduced into the garnet electrolyte|cathode interface and the pores of the cathode to reduce the impedance as well as to improve the electrochemical performance and maintain the intrinsic safety of the cell (Fig. 1a,b). In our work, the (Li,K,Cs)FSI molten salt with high ionic conductivity was chosen as an ideal catholyte because it demonstrated an ultra-low melting point of ~ 45°C compared with other reported inorganic molten salt systems[34]. In contrast to liquid electrolyte, this inorganic eutectic salt can guarantee better safety in the battery. The preparation of (Li,K,Cs)FSI molten salt can be facilely achieved by manual grinding and then simple heating (Supplementary Fig. 1). Optical images of four stages are presented in Fig. 2a. Concretely, powder mixture containing LiFSI, KFSI and CsFSI, according to the optimum molar ratio[37] of 30:35:35 from phase diagram (Supplementary Fig. 2) was heated and

transformed completely into molten salts with a certain of viscosity. The system returned back to solid state finally through a long period of natural cooling at ambient temperature.

Differential scanning calorimetry (DSC) was applied to accurately measure the phase transition temperature of ternary eutectic system, showing an ultra-low melting point ~ 45°C for the salt mixture (Fig. 2b). X-ray diffraction (XRD) patterns of LiFSI, KFSI, CsFSI and eutectic powder were shown in Supplementary Fig. 3a to identify the structure information. Scanning electron microscope (SEM) measurements were performed to reveal the micro morphology of eutectic salts (Supplementary Fig. 3b). To verify the thermal stability of molten salts, the glass fiber separator soaked with molten salts showed no trace of flame under fire burning (Supplementary Fig. 3c), demonstrating much more excellent flame retardancy and operation ability at high temperature than liquid electrolyte.

In addition, electrochemical impedance spectroscopy (EIS) results for molten salts were collected at the temperature range from 10 to 80°C (Supplementary Fig. 3d) and the Arrhenius plot was fitted according to the calculated σ and T (Fig. 2c). To be specific, the ionic conductivity of the molten salts at 45°C is 1.9 × 10^{-4} S cm^{-1} and it increases to 6.6 ×10^{4} S cm^{-1} at 60°C. Liner sweep voltammetry (LSV) was implemented to determine the electrochemical window, which is to say the ability to resist oxidation and reduction. The (Li,K,Cs)FSI ternary system electrolyte can maintain its antioxidation ability at a threshold voltage of up to 4.5 V versus Li^{+}/ Li at 60°C (Fig. 2d), which endows the qualification to match the ISE with high-voltage cathode to further increase the energy density.

Garnet electrolyte ($Li_{6.4}La_3Zr_{1.4}Ta_{0.6}O_{12}$, LLZTO) was prepared by solid-state reaction. The structure and morphology information are shown in Supplementary Fig. 4a, b. XRD patterns of both LLZTO powder and pellet are coincided with the standard cubic garnet phase (JCPDS No.45–0109) without any impurity peak. Besides, the optical image and the micro view of LLZTO powder, polished surface and cross section of LLZTO pellet are shown in Supplementary Fig. 4b. The ionic conductivity of the sintered LLZTO pellet is about 4.0 × 10^{-4} S cm^{-1} at 25°C and the impedance spectra of ceramic pellets at the temperature range of 20 to 80°C are presented in Supplementary Fig. 4c. The calculated activation energy (E_a) according to the fitted Arrhenius curve is 0.43 eV (Supplementary Fig. 4d). Lithium symmetric battery was also tested to reveal the impedance of garnet electrolyte|Li interface at RT, 45°C, 60°C and 80°C (Supplementary Fig. 5a). To eliminate the adverse effect of surface contamination Li_2CO_3/LiOH and further improve the lithiophilic of LLZTO, artificial gold interlayer was sputtered on the thoroughly polished garnet electrolyte pellet[38, 39]. Attributed to the enhanced wettability between Li_xAu and garnet electrolyte, the interfacial impedance corresponding to the small semi-circles are 34.2 Ω, 6.1 Ω, 3.5 Ω, 0.78 Ω at RT, 45°C, 60°C and 80°C respectively, meaning negligible anodic interfacial impedance and it presents high critical current density and stable deposition/stripping performance (Supplementary Fig. 5b–d).

Microstructure of the interfaces at the composite cathode

Next, half cells were assembled and characterized, with the typical configuration of lithium metal anode, LLZTO solid electrolyte and LFP/LFMP cathode (Fig. 1b). Specially, the polished LLZTO pellet with single-sided gold layer was immersed in molten lithium to prepare Li anode. A trace amount of molten salt (~ 5 μL cm^{-2}) was then coated on another side of LLZTO pellet, followed by attaching the cathode pieces.

As shown in the across section SEM images, an intimate contact was achieved between cathode and garnet electrolyte (Fig. 3a, b). Besides, the cathode particles were uniformly covered by the molten salts (Fig. 3f) in comparison with the isolated particles in the pristine cathode (Fig. 3g). Furthermore, energy dispersive spectrometer (EDS) mapping was performed to discern the distribution of the main elements. As indicated in Fig. 3c, d, lanthanum (La) coming from LLZTO electrolyte and iron (Fe) belonging to $LiFePO_4$ have an obvious dividing line. The sulfur (S) from FSI^- were abundant in cathode side (Fig. 3e), manifesting that molten salts penetrated the voids and pores of cathode sufficiently. In addition, commercial cathode piece with the infiltration of molten salts showed a more continuous connection within particles (Fig. 3h) than the pristine thick cathode (Supplementary Fig. 6). Thus, (Li,K,Cs)FSI filled in the cathode could provide a fast ion transport pathway for Li^+ and relieve the large overpotential as well as unsatisfactory capacity output at high charge/discharge rate.

X-ray photoelectron spectroscopy (XPS) was employed to detect the component of cathode electrolyte interlayer (CEI) of LFP after long battery cycling. In contrast to the XPS signals of pristine eutectic salts (Fig. 3i, k), enhanced LiF signal intensity (685.0 eV) and faint C–N (401.5 eV) and Li_3N (398.6 eV) signals were captured (Fig. 3j, l)[40, 41], proving good electrochemical stability of solvent-free molten salts.

Electrochemical performances of the solvent-free Li-metal batteries

As shown in Fig. 4a, the EIS spectra of Li||LFP cells consist of an intersection with real axis at high frequency, representing the total resistance of electrolyte, a semicircle at medium frequency corresponding to interfacial impedance and a slash related to diffusion of Li-ion at low frequency. Because of the enhanced wettability of LLZTO and lithium metal with the assistance of Au layer, the interfacial impedance of half cells referred to the semicircles at medium frequency can almost be ascribed to the contribution of cathode side that is 212.2 Ω, 42.7 Ω and 19.6 Ω at 45°C, 60°C and 80°C. The cells using molten salts showed total impedance of 294.5 Ω, 79.8 Ω and 37.0 Ω at these three temperatures respectively, which are close to the counterpart using liquid electrolytes and are much lower than the cell without any modification (Supplementary Fig. 7a, b). The remarkably reduced resistance is attributed to the conformal garnet electrolyte|cathode interface with the aid of high ionic conductive molten salts.

The imitate contact could guarantee improved electrochemical performances for QSSLMBs. Figure 4b and 4c show the charge-discharge curves and rate capability for the Li||LFP half cells with active mass loading ~ 3.3 mg cm^{-2} under various C-rates at 60°C. The cells with molten salts modified cathode interface exhibit good rate capacity with a low polarization and deliver a high discharge capacity of 163.8

mAh g^{-1}, 159.6 mAh g^{-1}, 155.4 mAh g^{-1}, 152.9 mAh g^{-1} and 145.1 mAh g^{-1} for 0.1, 0.3, 0.5, 1 and 2 C respectively. Enhanced rate capacity was also detected at 80°C, as illustrated in Supplementary Fig. 8a, b. The LFP cathode with active mass loading ~ 3.8 mg cm^{-2} was cycled at 0.5 C and 60°C, demonstrating a high capacity retention of 80.4% after 600 cycles, which is much more stable than the counterpart with liquid electrolyte suffering from serious capacity decay (Fig. 4d). Moreover, half cells can also stably cycle at a high rate of 1 C and maintain superior capacity of 81.4% after 1000 cycles (Fig. 4e). The Li||LFP cells were tested at 45°C and 80/100°C as well to confirm the low melting point and excellent thermal stability (Fig. 4f). The cells can output the capacity up to 153.3 mAh g^{-1} initially and is able to retain 83.8% of the capacity after 200 cycles at 0.5 C, compared to the similar battery performance with liquid electrolyte at 45°C (Fig. 4f and Supplementary Fig. 9). Exhilaratingly, LFP half cells could work stably for 200 cycles at very high temperature of 100°C (Fig. 4f). These superior performances are benefiting from the conformal interface and fast ion transport by the modification of molten salts with good thermal stability in the composite cathode.

Furthermore and importantly, commercial cathode pole pieces with high areal capacities could be directly adopted with molten salts strategy to ameliorate the energy density of solid-state batteries. Commercial LFP cathode with area capacity of ~ 2 mAh cm^{-2} were stably operated at 0.1 C and 0.2 C for 60°C or 80°C with near fully utilized capacity and slight fade at each rotation for 100 cycles (Fig. 4g), which is on account of the fast ion transport pathway established by molten salt (Fig. 3h). It is worth noting that direct use of commercial electrodes without extra adjustment could save the cost of production line transformation during the transition from LIBs to SSLMBs and quickly realize the industrialization of solid-state batteries.

Moreover, high voltage cathode was employed in our QSSLMBs, which can boost energy density. The LFMP cathodes with active mass loading ~ 3.1 mg cm^{-2} and cut-off voltage range of 2.5 to 4.5 V were collocated with garnet electrolyte. The rate performance and detailed charge/discharge profiles from 0.1 to 1 C at 60°C with acceptable voltage hysteresis were shown in Fig. 5a, b. Long-cycling tests illustrate an initial capacity of 135.8 mAh g^{-1} and 150.2 mAh g^{-1} at 0.5 C and maintained the capacity retention of 85.9% and 92.6% at the 100th cycle for 45°C and 60°C, respectively (Fig. 5c, Supplementary Fig. 10). The high voltage threshold of molten salts ensures the implementation of envisage of combining the ISE with high voltage cathode, much superior to those interlayers, like polyethylene oxide (PEO) with inferior antioxidant ability.

Various strategies on improving electrochemical performances of garnet electrolyte-based SSLMBs have been proposed, such as adding liquid electrolyte, polymer interlayer and composite electrolytes. We compared our batteries with literature from the aspect of working temperature, active mass loading/area capacity, rate capacity and cycling life, as shown in Fig. 5d and Supplementary Table 1. According to the summary data listed above, batteries with molten salts are superior to those with previously reported strategies and achieve outstanding comprehensive performance, including high area capacity, matching high voltage cathode, wide working temperature and long cycling life. Besides, we propose that

(Li,K,Cs)FSI could be applied in other oxide solid electrolyte including $Li_{1.5}Al_{0.5}Ge_{1.5}(PO_4)_3$ (LAGP) or $Li_{0.34}La_{0.56}TiO_3$ (LLTO) to relieve the interfacial problem. We also assume that (Li,K,Cs)FSI could play a role in potassium solid-state battery and might be a potential Na-ion conductor by facilely replacing LiFSI/KFSI with NaFSI. Such ternary molten salts have lower melting point than binary systems and are much more advantageous apparently in practical applications.

Simulation on the cells with and without molten salts

Last, finite element modeling was conducted to analyze the concentration polarization and overpotential during discharge through COMSOL Multiphysics (Supplementary Fig. 11a). Two models were established according to the experiment data of half cells modified by PEO-LiTFSI (Model 1) and the molten salts (Model 2) interlayer. According to the Warburg impedance in the EIS spectra of half cells with these two catholytes, the apparent ion diffusion coefficient D_{Li^+}were 6.82×10^{-14} cm^2 s^{-1} and 2.65×10^{-13} cm^2 s^{-1} for PEO-LiTFSI and molten salts schemes respectively (Supplementary Fig. 11b, c). With the assistance of high ion-conductive and diffusive catholyte, Model 2 could achieve a higher discharge platform and uniform distribution Li-ions in the cathode particles, in contrast to the counterpart (Model 1) with lower output voltage and distinct concentration polarization (Fig. 5e, f and Supplementary Fig. 11d). Therefore, rational design of composite cathode with fast and continuous ion transport pathway is essential to attain SSLMBs with better electrochemical performances.

In summary, we report a solvent-free, high-performance, ceramic-based Li-metal batteries by adding an interlayer of a ternary eutectic electrolyte (Li,K,Cs)FSI. The molten salt electrolyte held extremely low eutectic transition temperature of ~ 45°C, wide electrochemical window (> 4.5 V vs. Li^+/Li) and high ionic conductivity ~ 6.6×10^{-4} S cm^{-1} at 60°C along with good thermal stability. Through adding tiny molten salt as an interface layer to substitute intimate binding for point contact, the solvent-free Li metal batteries can stably work at the temperature range of 45 to 100°C. The LFP cathode showed high capacity retention of 83.8% and 81.4% after 200 and 1000 cycles at 45°C and 60°C respectively. Besides, high area capacity LFP cathode (~ 2 mAh cm^{-2}) and high voltage cathode LFMP (2.5–4.5 V) were applied to further enhance the energy density of solid-state batteries. Importantly, commercial electrode pieces could be used directly without extra modification. Finite element analysis also confirmed that high ionic conductivity and rapid diffusion inside cathode could relieve the large overpotential and concentration polarization, further contributing to performance output. This work affords a novel strategy to address the interfacial problems and shows bright prospect in the high-performance SSLMBs with low cost.

Methods

Preparation of garnet electrolyte

The cubic garnet-structure $Li_{6.4}La_3Zr_{1.4}Ta_{0.6}O_{12}$ powder was prepared by the solid-state reaction. Specifically, the raw materials of $LiOH•H_2O$ (20% excess to compensate for Li loss), La_2O_3, ZrO_2 and

Ta_2O_5 were mixed and ball-milled according to the stoichiometric ratios with isopropyl alcohol for 600 rpm 5 h, followed by sintering in air atmosphere at 950°C for 6 h to form the cubic LLZTO powder. Synthetic LLZTO powder was ground with 2 wt% Al_2O_3 as sintering aid and then was pressed into pellets with approximate 1 mm in thickness and 12 mm in diameter at 4 MPa. Subsequently, these pellets were sintered in MgO crucible at 1250°C for 40 min to form dense ceramic pellets. The as-prepared ceramic pellets were polished with 180, 800, 2000 mesh sandpapers to remove impurities on surface and were transferred immediately into argon globe box for the following experiments.

Preparation of (Li,K,Cs) molten salt electrolyte

The starting materials used for the synthesis of (Li,K,Cs)FSI were LiFSI (98%, Aladdin), KFSI (98%, Macklin), and homemade CsFSI, which was synthesized through double replacement reaction of LiFSI and CsF (99%, Macklin) in ethanol solvent, followed by centrifugation, recrystallization and drying. All precursors were dried at 60°C in vacuum drying oven and argon box to remove the trace moisture before use. LiFSI, KFSI and CsFSI in the molar ratio of 30:35:35 according to phase diagram were ground and mixed in mortar for 30 min. They were then collected into vial and heated at 60°C for 1 h to conduct eutectic reaction sufficiently. The obtained molten salts were naturally cooled for preservation, ground into powder when characterizing, and reheated to 60°C in battery assembly.

Preparation of LFP and LFMP cathode

Both LFP and LFMP cathode with active material loading ~ 3 mg cm^{-2} were prepared by mixing the active material, Super P and PVDF at a weight ratio of 8:1:1 and were then added N-1-methyl-2-pyrolidone to form homogeneous slurry through THINKY MIXER. The slurry was then doctor bladed on a carbon-coated aluminum foil and was dried at 60°C for 12 h in vacuum oven. LFP electrodes with area capacities about 2 mAh cm^{-2} were purchased directly from Canrd New Energy Technology. All the LFP electrode foil was cut into pole pieces with a diameter of 8 mm and thoroughly dried in the glove box before use.

Characterizations

Crystal structure patterns of samples were collected through Bruker D8 Advance using a Cu Kα X-ray radiation source with the 2θ range from 10° to 80°. SEM and EDS mapping were performed on a JEOL JSM-7800F Prime to visualize the micro morphology and the element distribution. The chemical state and bonding information were characterized by XPS (Thermo Fisher ESCA 250XI) using Al Kα radiation (λ = 0.83 nm, hv = 1486.7 eV) and the X-ray source was operated at 2 kV and 20 mA. Molten salts & LFP specimen was analyzed after washing with diethyl carbonate solvent to fully expose the surface of electrode particles. DSC test was carried out on a DSC 8000 (PerkinElmer) with the temperature range from 0 to 80°C at a temperature scanning rate of 2°C min^{-1} under N_2 atmosphere.

Electrochemical measurements

Electrochemical impedance spectroscopy (EIS) analysis was conducted on the Biologic VSP-300 workstation from 20 to 80°C with the frequency range of 7 MHz to 100 mHz and 10 mV amplitude. Thin

gold layers were sputtered on both sides of LLZTO pellet to act as blocking electrodes for ion conductivity test. Glass fiber separator with 16 mm in diameter and 0.18 mm in thickness was immersed in molten salts for EIS test at elevated temperatures from 10 to 80°C. Both systems were sandwiched by two pieces of stainless steel (SS) and assembled into CR2032-type coin cells. The ionic conductivity (σ) was calculated by the following equation:

$$\sigma = \frac{\mathrm{L}}{\mathrm{R}\times\mathrm{S}}$$

where L represents the thickness of the electrolytes, R is the impedance at different temperatures, S is the contact area between electrolyte and blocking electrode.

Liner sweep voltammetry (LSV) was carries out to analyze the electrochemical stability of molten salts. Li/glass fiber separator & molten salts/SS cells were employed to measure its electrochemical window. The scan rate was 1 mV s^{-1} with an anodic scan from open circuit voltage (OCV) to 5 V versus Li^+/Li.

To evaluate electrochemical performance of batteries, CR-2032 type cells were assembled with LFP/LFMP cathode, tiny of molten salts (the calculated specific volume was ~ 5 μL cm^{-2} according to the state at 60°C, LLZTO pellet and lithium anode. In order to improve the wettability between garnet electrolyte and lithium metal, thin gold layer was sputtered on one side of ceramic pellets, followed by molten lithium spreading out the surface of LLZTO at ~ 300°C in Ar-filled glovebox. To eliminate the possibility of direct contact between molten salts and lithium, cathode is placed at the bottom of the coin cell during test. For the counterpart with liquid electrolyte, the dosage of $LiPF_6$ (EC: DEC = 1:1 vol%) is 10 μL. Galvanostatic cycling was tested on LAND battery system at 45°C, 60°C and 80°C in environmental chamber with the cut-off voltage of 2.5 to 4.0 V for LFP and 2.5 to 4.5 V for LFMP cathode. As for the test at 100°C, the voltage range of LFP was changed to 2.8–4.0 V. For the rate performance test, half cells were cycled at 0.1 C, 0.3 C, 0.5 C, 1 C and 2 C for 5 cycles respectively. As for symmetric lithium batteries, LLZTO pellets with Au coated on both sides were covered with molten lithium and then were cycled at assigned current density and temperature.

Finite element simulation

Apparent lithium-ion diffusion coefficient ($\mathrm{D}_{\mathrm{Li}^+}$) was calculated through the Warburg impedance (Z_w) in the EIS spectra according to the following equation:

$$D_{\mathrm{Li}^+} = \frac{T^2R^2}{2A^2n^4F^4C^2\sigma^2}$$

where R is the gas constant (8.314 J mol^{-1} K^{-1}), T is the thermodynamic temperature (333.15 K), A is the area of cathode (cm^2), n represents the electron transfer number in redox process (n = 1 for $LiFePO_4$), F is the Faraday constant (96485 C mol^{-1}), C is the molar concentration of Li-ion in $LiFePO_4$ (2.28 × 10^{-2} mol cm^{-3}) and σ is the Warburg factor fitted through the Z'-$\omega^{-1/2}$ curve shown above. The $\mathrm{D}_{\mathrm{Li}^+}$calculated

through the equation for the LFP with molten salts or PEO-LiTFSI film strategy are 2.65 × 10^{-13} cm^2 s^{-1} and 6.82 × 10^{-14} cm^2 s^{-1} respectively.

For finite element analysis, Model 1 represents the half cell modified by PEO-LiTFSI (EO: Li^+ = 16:1) with low σ and D_{Li^+} and Model 2 represents the half cell with molten salts with higher σ and D_{Li^+}. As for Model 1 with PEO-LiTFSI, the electrolyte conductivity parameter σ of catholyte in the simulation was set to 1.6 × 10^{-4} S cm^{-1} and the $D_{Li^+}$was 6.82 × 10^{-14} cm^2 s^{-1} at 60°C. With regard to Model 2, the σ of catholyte was 6.6 × 10^{-4} S cm^{-1} because of the infiltration of molten salts into cathode and the $D_{Li^+}$was 2.65 × 10^{-13} cm^2 s^{-1}. The discharge current density was set to 0.3 mA cm^{-2} for both models and the arrows in the simulation represent the direction of the current.

Data availability

All data generated and analyzed during this study are included in the article and its Supplementary Information file. The detailed data for the study is available from the corresponding author upon reasonable request.

References

1. Manthiram, A., Yu, X. & Wang, S. Lithium battery chemistries enabled by solid-state electrolytes. Nat. Rev. Mater. **2**, 16103 (2017).
2. Choi, J.W. & Aurbach, D. Promise and reality of post-lithium-ion batteries with high energy densities. Nat. Rev. Mater. **1**, 16013 (2016).
3. Zhao, Q., Stalin, S., Zhao, C.-Z. & Archer, L.A. Designing solid-state electrolytes for safe, energy-dense batteries. Nat. Rev. Mater. **5**, 229–252 (2020).
4. Zheng, Y. et al. A review of composite solid-state electrolytes for lithium batteries: fundamentals, key materials and advanced structures. Chem. Soc. Rev. **49**, 8790–8839 (2020).
5. Zhang, Z. et al. New horizons for inorganic solid state ion conductors. Energy Environ. Sci. **11**, 1945–1976 (2018).
6. Ji, X. et al. Advanced inorganic/polymer hybrid electrolytes for all-solid-state lithium batteries. J. Adv. Ceram. **11**, 835–861 (2022).
7. Liu, J. et al. Pathways for practical high-energy long-cycling lithium metal batteries. Nat. Energy **4**, 180–186 (2019).
8. Randau, S. et al. Benchmarking the performance of all-solid-state lithium batteries. Nat. Energy **5**, 259–270 (2020).
9. Gao, Z. et al. Promises, Challenges, and Recent Progress of Inorganic Solid-State Electrolytes for All-Solid-State Lithium Batteries. Adv.Mater. **30**, 1705702 (2018).
10. Gonzalez Puente, P.M. et al. Garnet-type solid electrolyte: Advances of ionic transport performance and its application in all-solid-state batteries. J. Adv. Ceram. **10**, 933–972 (2021).

11. Wu, J., Liu, S., Han, F., Yao, X. & Wang, C. Lithium/Sulfide All-Solid-State Batteries using Sulfide Electrolytes. Adv.Mater. **33**, 2000751 (2021).
12. He, W. et al. Space Charge Layer Effect in Sulfide Solid Electrolytes in All-Solid-State Batteries: In-situ Characterization and Resolution. Trans. Tianjin Univ. **27**, 423–433 (2021).
13. Li, X. et al. Progress and perspectives on halide lithium conductors for all-solid-state lithium batteries. Energy Environ. Sci. **13**, 1429–1461 (2020).
14. Liu, J., Wang, S., Qie, Y. & Sun, Q. Identifying lithium fluorides for promising solid-state electrolyte and coating material of high-voltage cathode. Mater. Today Energy **21** (2021).
15. Famprikis, T., Canepa, P., Dawson, J.A., Islam, M.S. & Masquelier, C. Fundamentals of inorganic solid-state electrolytes for batteries. Nat. Mater. **18**, 1278–1291 (2019).
16. Liu, J. et al. Unlocking the Failure Mechanism of Solid State Lithium Metal Batteries. Adv. Energy Mater. **12**, 2100748 (2021).
17. Wang, D.W., Zhu, C.B., Fu, Y.P., Sun, X.L. & Yang, Y. Interfaces in Garnet-Based All-Solid-State Lithium Batteries. Adv. Energy Mater. **10**, 2001318 (2020).
18. Wang, C. et al. Garnet-Type Solid-State Electrolytes: Materials, Interfaces, and Batteries. Chem. Rev. **120**, 4257–4300 (2020).
19. Indu, M.S., Alexander, G.V., Sreejith, O.V., Abraham, S.E. & Murugan, R. Lithium garnet-cathode interfacial chemistry: inclusive insights and outlook toward practical solid-state lithium metal batteries. Mater. Today Energy **21** (2021).
20. Qin, Z. et al. Fast Li-ion transport pathways via 3D continuous networks in homogeneous garnet-type electrolyte for solid-state lithium batteries. Energy Storage Mater. **43**, 190–201 (2021).
21. Bi, Z.J. et al. Dual-interface reinforced flexible solid garnet batteries enabled by in-situ solidified gel polymer electrolytes. Nano Energy **90**, 106498 (2021).
22. Han, F.D. et al. Interphase Engineering Enabled All-Ceramic Lithium Battery. Joule **2**, 497–508 (2018).
23. Zhong, G. et al. Rapid, high-temperature microwave soldering toward a high-performance cathode/electrolyte interface. Energy Storage Mater. **30**, 385–391 (2020).
24. Tan, D.H.S. et al. Carbon-free high-loading silicon anodes enabled by sulfide solid electrolyte. Science **373**, 1494–1499 (2021).
25. Kwak, H. et al. New Cost-Effective Halide Solid Electrolytes for All-Solid-State Batteries: Mechanochemically Prepared Fe^{3+}-Substituted Li_2ZrCl_6. Adv. Energy Mater. **11**, 2003190 (2021).
26. Zhao, C.-Z. et al. Liquid phase therapy to solid electrolyte–electrode interface in solid-state Li metal batteries: A review. Energy Storage Mater. **24**, 75–84 (2020).
27. Bates, A.M. et al. Are solid-state batteries safer than lithium-ion batteries? Joule **6**, 742–755 (2022).
28. Yu, C.Y., Choi, J., Han, J., Lee, E. & Kim, J.H. Phase Stability of Garnet Solid-Electrolyte Interfacing with Various Cathodes in All-Solid-State Batteries. J. Electrochem. Soc. **169**, 020520 (2022).
29. Park, K. et al. Electrochemical Nature of the Cathode Interface for a Solid-State Lithium-Ion Battery: Interface between $LiCoO_2$ and Garnet-$Li_7La_3Zr_2O_{12}$. Chem. Mater. **28**, 8051–8059 (2016).

30. Navarrete, N. et al. Thermal energy storage of molten salt –based nanofluid containing nano-encapsulated metal alloy phase change materials. Energy **167**, 912–920 (2019).
31. Sun, G.T., Liu, Y.F., Dong, S. & Wang, J.M. Study on novel molten salt-ceramics composite as energy storage material. J. Energy Storage **28**, 101237 (2020).
32. Xiao, M. et al. Molten-Salt-Mediated Synthesis of an Atomic Nickel Co-catalyst on TiO_2 for Improved Photocatalytic H_2 Evolution. Angew. Chem. Int. Ed. **59**, 7230–7234 (2020).
33. An, M.N. et al. Low-Temperature Molten Salts Synthesis: $CsPbBr_3$ Nanocrystals with High Photoluminescence Emission Buried in Mesoporous SiO_2. ACS Energy Lett **6**, 900–907 (2021).
34. Zhang, S. et al. Liquid metal batteries for future energy storage. Energy Environ. Sci. **14**, 4177–4202 (2021).
35. Wang, K. et al. Lithium-antimony-lead liquid metal battery for grid-level energy storage. Nature **514**, 348–350 (2014).
36. Xiao, Y. et al. Electrolyte melt infiltration for scalable manufacturing of inorganic all-solid-state lithium-ion batteries. Nat. Mater. **20**, 984–990 (2021).
37. Kubota, K., Nohira, T. & Hagiwara, R. New inorganic ionic liquids possessing low melting temperatures and wide electrochemical windows: Ternary mixtures of alkali bis(fluorosulfonyl)amides. Electrochim. Acta **66**, 320–324 (2012).
38. Sharafi, A. et al. Surface Chemistry Mechanism of Ultra-Low Interfacial Resistance in the Solid-State Electrolyte $Li_7La_3Zr_2O_{12}$. Chem. Mater. **29**, 7961–7968 (2017).
39. Tsai, C.L. et al. $Li_7La_3Zr_2O_{12}$ Interface Modification for Li Dendrite Prevention. ACS Applied Materials & Interfaces **8**, 10617–10626 (2016).
40. Li, X., Zheng, Y. & Li, C.Y. Dendrite-free, wide temperature range lithium metal batteries enabled by hybrid network ionic liquids. Energy Storage Mater. **29**, 273–280 (2020).
41. Xue, W. et al. FSI-inspired solvent and “full fluorosulfonyl” electrolyte for 4 V class lithium-metal batteries. Energy Environ. Sci. **13**, 212–220 (2020).
42. Hu, B. et al. An in Situ-Formed Mosaic Li_7Sn_3/LiF Interface Layer for High-Rate and Long-Life Garnet-Based Lithium Metal Batteries. ACS Applied Materials & Interfaces **11**, 34939–34947 (2019).
43. Luo, W. et al. Reducing Interfacial Resistance between Garnet-Structured Solid-State Electrolyte and Li-Metal Anode by a Germanium Layer. Adv.Mater. **29**, 1606042 (2017).
44. Chi, S.S. et al. Solid polymer electrolyte soft interface layer with 3D lithium anode for all-solid-state lithium batteries. Energy Storage Mater. **17**, 309–316 (2019).
45. Zhou, W. et al. Plating a Dendrite-Free Lithium Anode with a Polymer/Ceramic/Polymer Sandwich Electrolyte. J. Am. Chem. Soc. **138**, 9385–9388 (2016).
46. Zhang, W., Nie, J., Li, F., Wang, Z.L. & Sun, C. A durable and safe solid-state lithium battery with a hybrid electrolyte membrane. Nano Energy **45**, 413–419 (2018).

47. Zhang, M. et al. Flexible, Mechanically Robust, Solid-State Electrolyte Membrane with Conducting Oxide-Enhanced 3D Nanofiber Networks for Lithium Batteries. Nano Lett. **21**, 7070–7078 (2021).
48. Wan, Z.P. et al. Low Resistance-Integrated All-Solid-State Battery Achieved by $Li_7La_3Zr_2O_{12}$ Nanowire Upgrading Polyethylene Oxide (PEO) Composite Electrolyte and PEO Cathode Binder. Adv. Funct. Mater. **29**, 1805301 (2019).
49. Yu, G. et al. Plasma optimized $Li_7La_3Zr_2O_{12}$ with vertically aligned ion diffusion pathways in composite polymer electrolyte for stable solid-state lithium metal batteries. Chem. Eng. J. **430**, 132874 (2022).
50. Guo, S. et al. Thin laminar inorganic solid electrolyte with high ionic conductance towards high-performance all-solid-state lithium battery. Chem. Eng. J. **427**, 131948 (2022).

Declarations

Acknowledgements

The authors gratefully acknowledge financial support from National Key Research and Development Program (2019YFA0210600) and Shanghai Rising Star Program (20QA1406600). The Center for High-resolution Electron Microscopy (C$\hbar$EM), SPST of ShanghaiTech University (#EM02161943), Shanghai Science and Technology Plan (21DZ2260400) was also acknowledged for support.

Author contributions

J.Y., W.L. conceived the idea and designed the experiments. J.Y., R.W., S.C., and Q.H., carried out the experimental work, including material synthesis and electrochemical measurements. C.Z and J.Y carried out the SEM experiments. C.W and J.Y conducted the XPS tests and data analysis. J.Y performed the finite element analysis. J.Y. and W.L. wrote the manuscript with input from all other co-authors.

Competing interests

The authors declare no competing interests.

Figures

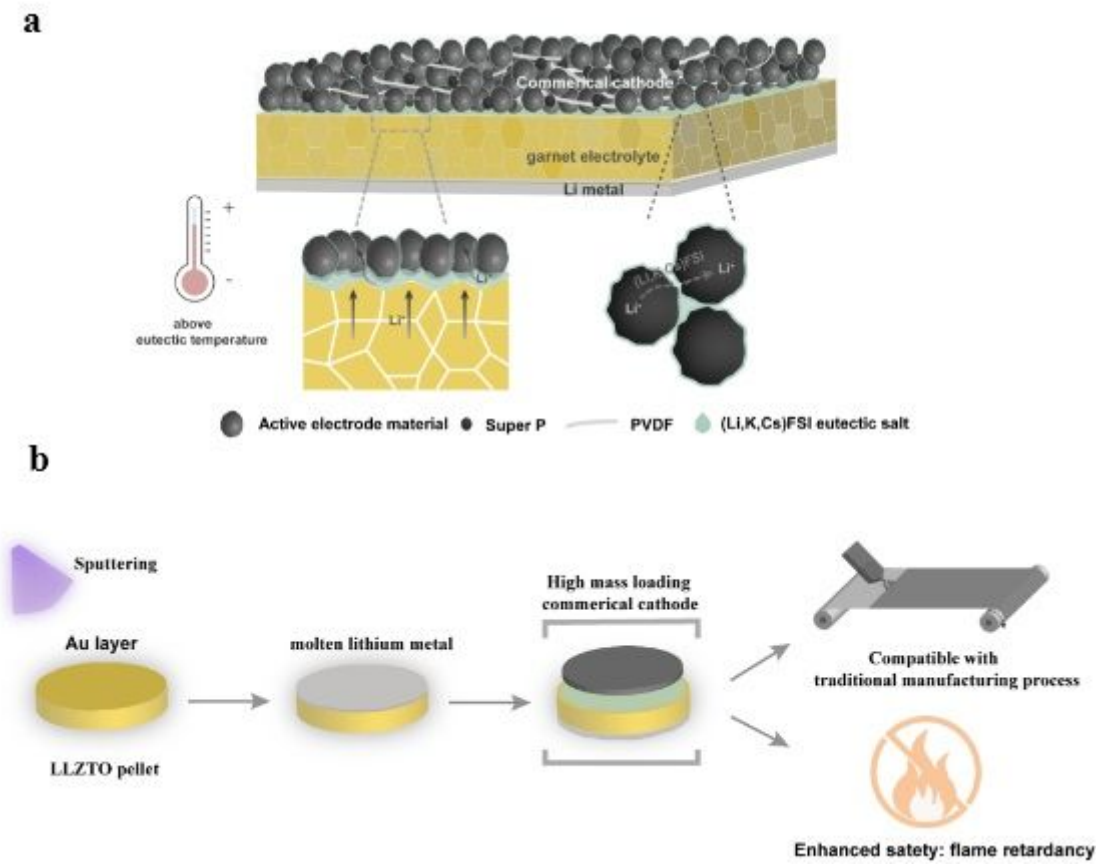

Figure 1

Schematic illustration and procedure process for the quasi-solid-state battery modified by (Li,K,Cs)FSI molten salt as catholyte at the electrolyte|cathode interface. a Structure for the solid-state battery with (Li,K,Cs)FSI molten salt. Molten salts could penetrate into the pores in cathode, enhancing the Li-ion transport and decreasing the charge transfer impedance above the eutectic transition temperature of the ternary salts, as well as reducing interfacial impedance at the electrolyte|cathode interface. **b** Flow chart of battery preparation procedure with molten salts and the advantages of ceramic-molten salt hybrid strategy for solid-state Li-metal batteries.

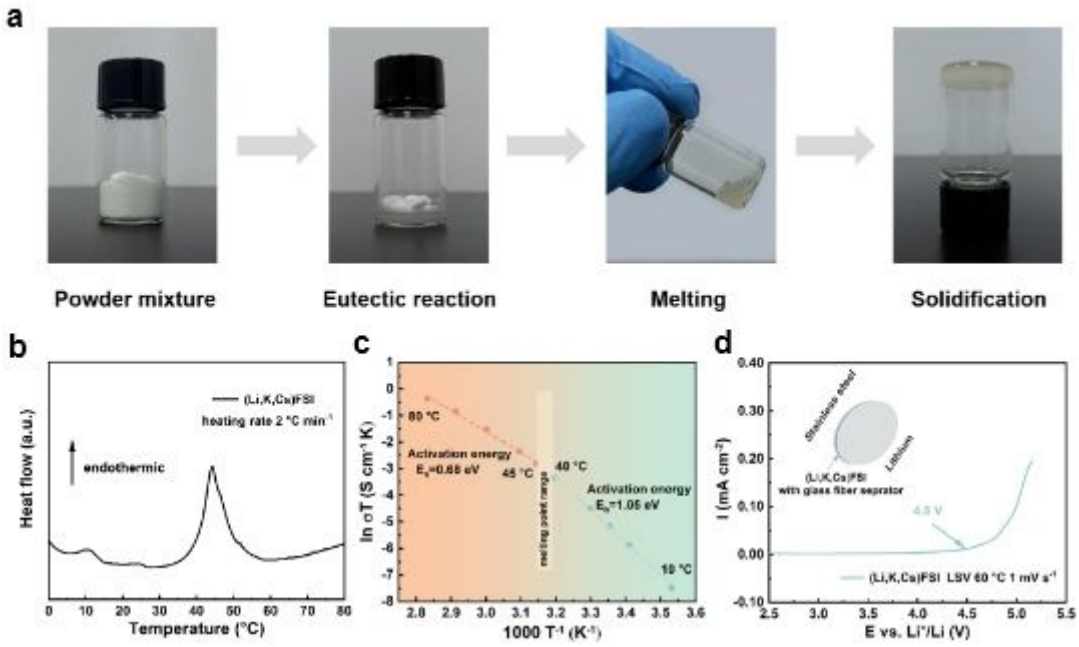

Figure 2

Physical and electrochemical properties of the (Li,K,Cs)FSI eutectic salt. a Four stages in the preparation of molten salts, including powder mixture, eutectic reaction, melting and solidification. **b** The DSC curve of (Li,K,Cs)FSI powder at a heating rate of 2 °C min^{-1}. **c** Arrhenius plots of the (Li,K,Cs)FSI electrolyte at the temperatures from 10 to 80 °C. **d** LSV curves of Li/ (Li,K,Cs)FSI/ SS cells at 60 °C with a scan rate of 1 mV s^{-1}.

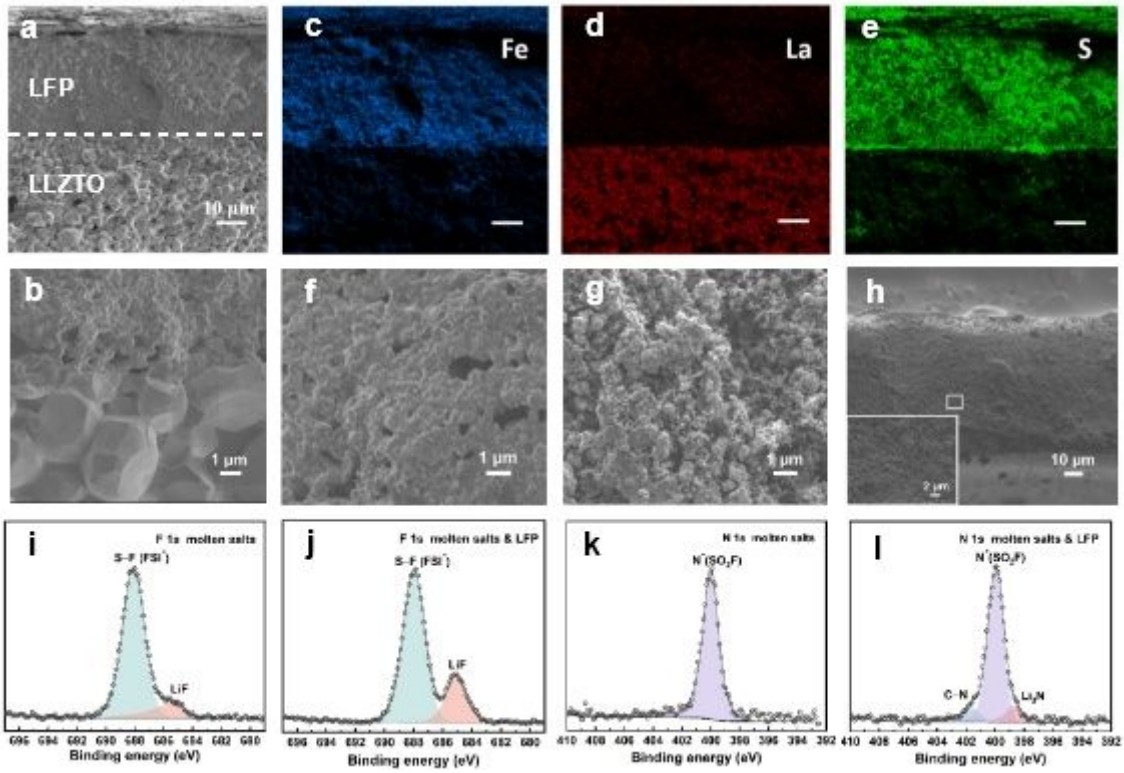

Figure 3

Morphology and structure characterization of the samples. a,b SEM images of cross-section of the electroyte|cathode interface (**a**) and the enlarged view (**b**). **c-e** Corresponding element mapping of Fe from LFP (**c**), La from LLZTO (**d**) and S from FSI^- (**e**). **f-h** SEM images of cathode particles with molten salts (**f**), the pristine cathode without molten salts (**g**) and the commercial thick cathode filled with molten salts **(h)**. **i-l** XPS signals of F 1s (**i,j**) and N 1s (**k,l**) for molten salt and the molten salts & LFP specimen after cycling.

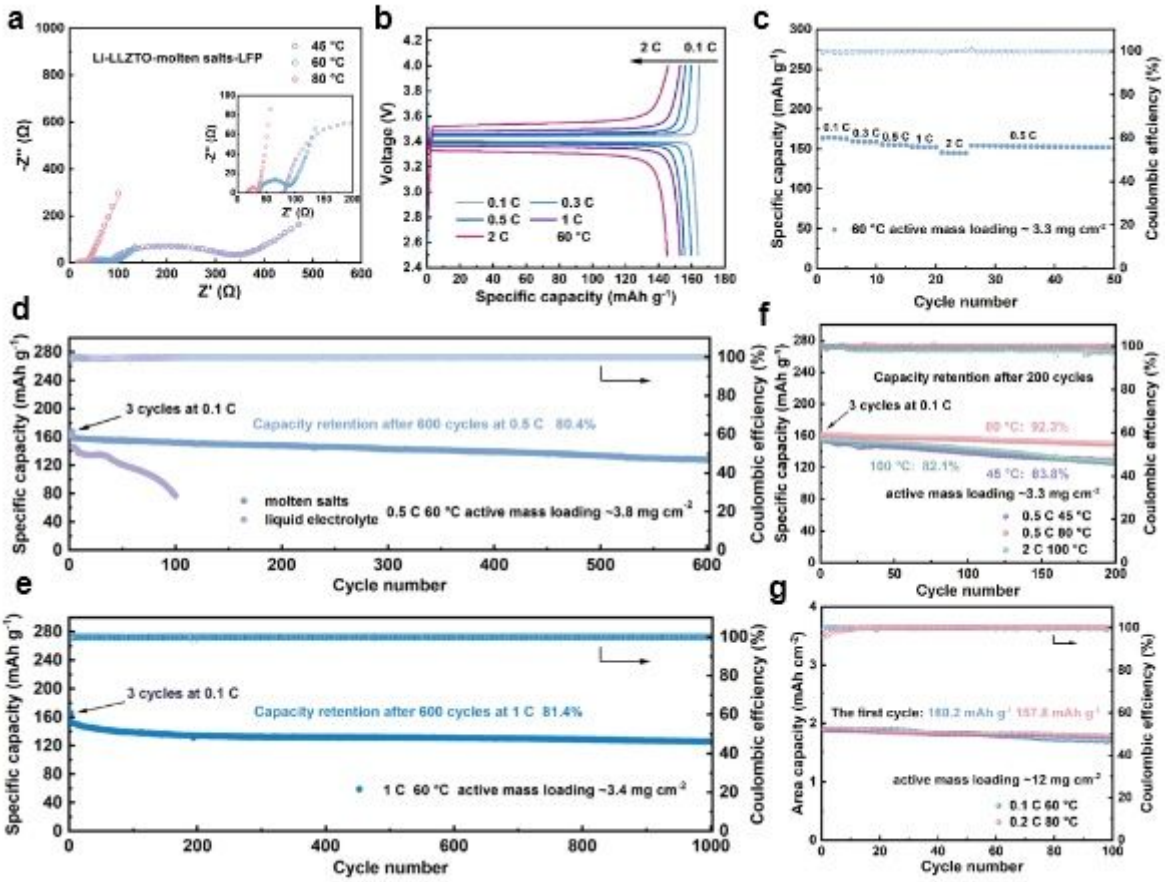

Figure 4

Electrochemical performance of the quasi-solid-state Li||LFP batteries modified by (Li,K,Cs)FSI molten salt as catholyte. a EIS spectra of Li||LFP half cell at 45 °C, 60 °C and 80 °C. **b,c** Rate performance of charge-discharge voltage profiles (**b**) and discharge capacities (**c**) from 0.1 to 2 C at 60 °C. **d** Cycling performance of the half cell at the C-rate of 0.5 C at 60 °C, compared with the cell using liquid electrolyte. **e** Long cycling performance at the C-rate of 1 C at 60 °C. **f** Cycling performance of the half cell at low-temperature of 45 °C and high-temperature of 80 °C and 100 °C. **g** Cycling performance of the cell using commercial LFP cathode with high mass loading ~12 mg cm^{-2}.

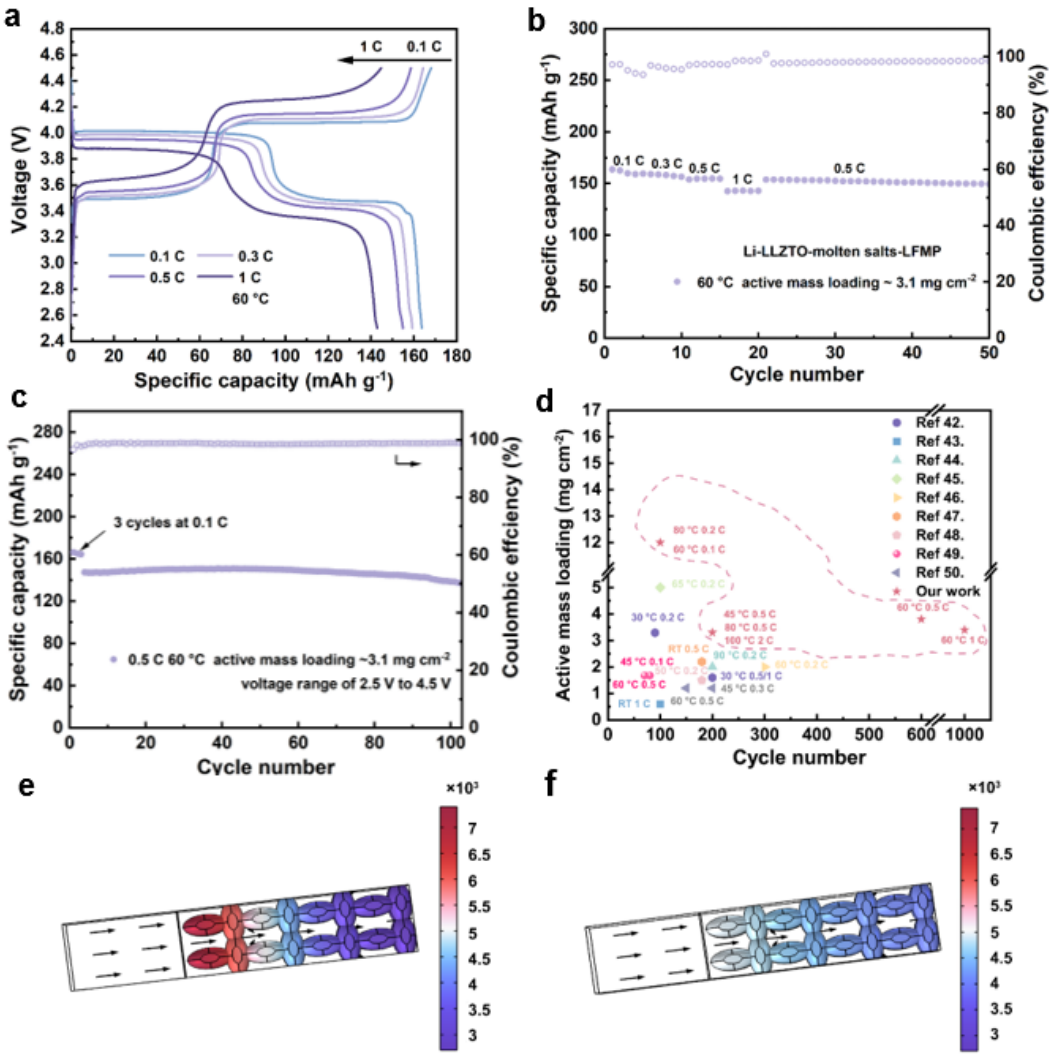

Fig. 5 | Electrochemical performance of the high voltage cathode LFMP (2.5 – 4 V), performance comparison and finite element analysis. a,b Rate performance of charge and discharge profiles (**a**) and discharge capacity (**b**) of different rates at 60 °C. **c** Long cycling of the cells tests at 60 °C. **d** Active mass loading and cycle number of the garnet-based SSLMBs in our work compared with reported literatures using various interface engineering strategies[42-50]. **e,f** Variation of Li-ion concentration on the surface of electrode particles through finite element analysis in Model 1 with low σ and D_{Li^+} (**e**) and Model 2 with high σ and D_{Li^+} (**f**).

Figure 5

See above image for figure legend.

Supplementary Files

This is a list of supplementary files associated with this preprint. Click to download.

- SupplementaryInformation.docx